JACS
JOURNAL OF THE AMERICAN CHEMICAL SOCIETY
pubs.acs.org/JACS
Article

Triggering Lattice Oxygen Release for Semiconducting Carbon Nanotube Array Synthesis

Zhe Liu, Hao Li, Zhisheng Peng, Mingzhi Zou, Zhenghang Yu, Yue Li, Zanlin Qiu, Xiucai Sun,* Liu Qian,* and Jin Zhang*

Cite This: J. Am. Chem. Soc. 2025, 147, 32752−32760
Read Online
ACCESS | Metrics & More | Article Recommendations | Supporting Information

ABSTRACT: Lattice oxygen in metal oxides offers potential pathways for advanced catalyst design, including catalysts for the selective growth of semiconducting single-walled carbon nanotubes (s-SWCNTs). In this study, an increase of lattice-oxygen release flux up to 10^5 is achieved via a lattice oxygen triggering (LOT) strategy for oxide catalysts. The LOT strategy is experimentally realized by ion implantation of titanium (Ti) and iron (Fe) elements into the sapphire substrate, followed by an annealing process for Ti migration onto the surface and Fe stable substitution in the sapphire lattice. The LOT process occurs when Fe atoms dope into Ti oxides, forming the catalysts for SWCNT growth. The continuously released lattice oxygen serves as an in situ etchant for precise removal of metallic tubes, resulting in the direct synthesis of horizontally aligned s-SWCNT arrays with >98% purity. Field-effect transistors based on the s-SWCNT arrays exhibit ultralow subthreshold swing of 60 mV dec^{-1}, and high carrier mobility of 2291 $cm^2 \cdot V^{-1} \cdot s^{-1}$. This LOT strategy establishes a paradigm for tuning lattice oxygen kinetics and thermodynamics, opening avenues for an oxygen-centric catalyst design in nanomaterial synthesis.

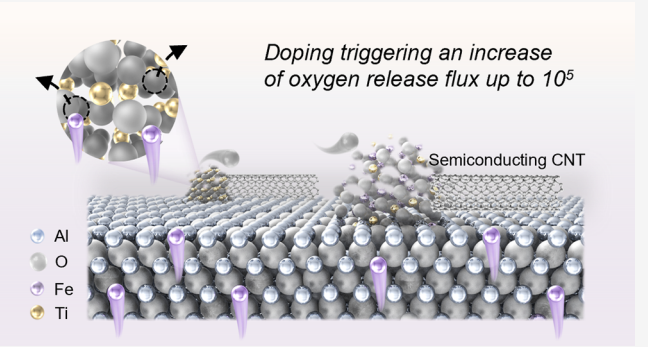

INTRODUCTION

Lattice oxygen in metal oxides has been widely researched, particularly in catalytic fields, as it provides abundant opportunities for material design. In the oxygen evolution reaction process, the thermodynamic instability of the oxygen anion in the metal oxide lattice, and the involvement and mobility of lattice oxygen were reported.[1,2] In acetylene conversion, lattice oxygen acts as the oxidant for preferential acetylene activation due to its high diffusion rate with metal oxides.[3] When it comes to the realm of photovoltaics, photoelectrochemical cells, and photocatalysis, lattice oxygen was also extensively investigated for modulating the activity of photocatalysts like titanium dioxide (TiO_2).[4−7] In addition, for controlled growth of carbon nanotubes (CNTs), lattice oxygen was regarded as an effective approach for selectively etching or preventing the formation of metallic CNTs.[8,9]

Horizontally aligned single-walled carbon nanotube (SWCNT) arrays hold significant promise for integrated circuits technology, due to their multiple advantages as one-dimensional Dirac materials.[10−13] Although the direct growth of SWCNT arrays achieves samples with higher quality, better alignment, and less contamination, the coexistence of metallic (m-) and semiconducting (s-) SWCNTs is still a major obstacle to their application in next-generation nanoelectronics,[14] which requires high-purity s-SWCNTs. Based on the electron density difference at the Fermi level of m-SWCNTs and s-SWCNTs, numerous studies have explored selective etching methods using oxygen, hydrogen, or other etchants during the chemical vapor deposition (CVD) growth process.[15−18] Notably, oxidative etching demonstrated remarkable effectiveness, in which water vapor achieved the etching of 80% m-SWCNTs ,[19] and the oxygen-assisted floating catalyst chemical vapor deposition process produced s-SWCNT networks with over 90% purity.[20] However, conventional oxidative etching introduces etchants throughout the growth atmosphere, leading to the complex coupling of etching conditions with the growth parameters and relatively low purity, commonly less than 95%.

Instead of feeding oxidative etchant, lattice oxygen from metal oxide nanoparticles, like TiO_2 or ZrO_2, enables precise etching of m-SWCNTs.[8] However, the control of lattice oxygen remains difficult. Doping has been proven as an effective method to achieve high oxygen vacancy concen-

Received: May 22, 2025
Revised: August 16, 2025
Accepted: August 19, 2025
Published: August 26, 2025

https://doi.org/10.1021/jacs.5c08656
J. Am. Chem. Soc. 2025, 147, 32752−32760

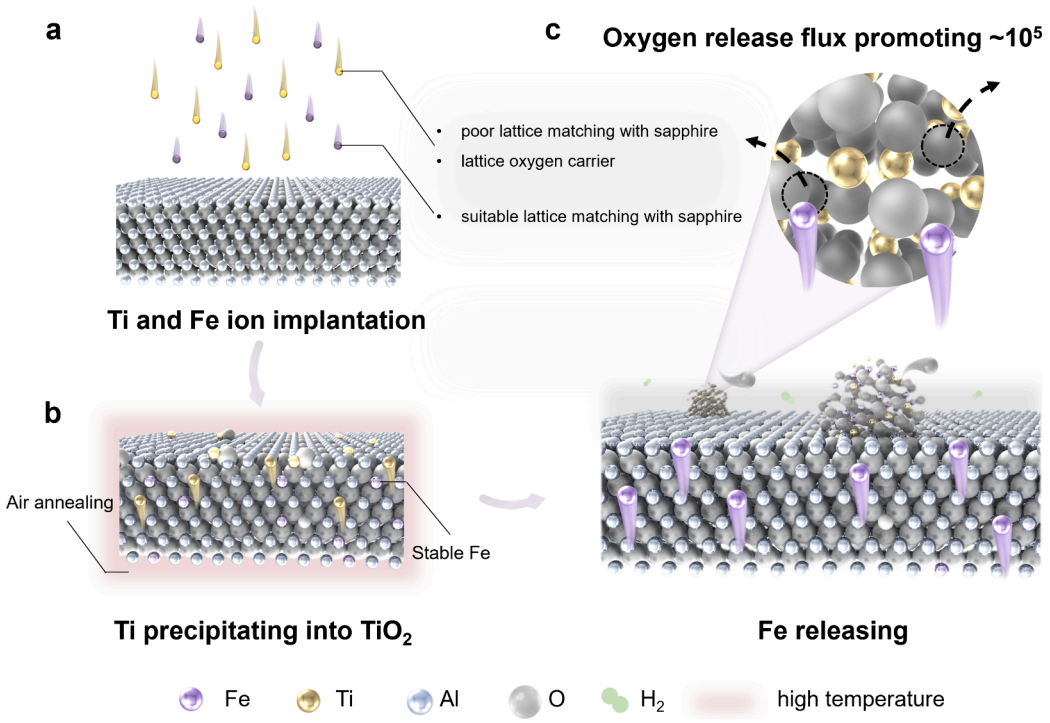

Figure 1. Detailed schematic diagram of the lattice oxygen triggering (LOT) strategy for promoting lattice oxygen release. (a) Selection principle of ion implantation elements. (b) Air-annealing induced Ti atoms migration and precipitation toward the substrate surface into TiO_2. Fe atoms remain embedded in the substrate. (c) Fe releasing process under hydrogen atmosphere, inducing doping of TiO_2 and lattice oxygen release.

tration, addressing the insufficient and noncontinuous oxygen release from pure TiO_2.[21−23] Various dopants have been investigated, in which low-valence transition metal dopants particularly show promise for creating oxygen vacancies in TiO_2 through charge compensation mechanisms.[24−26] Furthermore, Fe^{3+} doping significantly improves the capacity of oxygen-release when substituting Ti^{4+} in TiO_2 lattices because of their comparable ionic radii.[27] Therefore, if Fe^{3+} doping can be successfully introduced during CNT growth using TiO_2 as the catalyst, a more precise control can be realized for s-SWCNT enrichment. This process necessitates developing alternative catalyst fabrication strategies that synchronize doping with CNT growth, rather than conventional preloading methods. Ion implantation emerges as a viable technique for in situ catalyst nanoparticle formation[28,29] with improved uniformity,[30] while avoiding the "self-purification" effect from predoping catalysts.[31] Based on ion implantation, we propose a lattice oxygen triggering (LOT) strategy to achieve controlled lattice oxygen release via Fe doping into Ti oxide catalysts and to realize precise and effective etching of m-SWCNTs.

Figure 1a−c schematically illustrates the complete process of our LOT strategy. Initially, Ti and Fe ions are implanted into the sapphire substrate. During air annealing, Ti atoms migrate and precipitate toward the substrate surface due to poor lattice matching with sapphire, ultimately transforming into TiO_2. In contrast, Fe atoms remain embedded within the substrate, maintaining thermodynamic stability because of structural compatibility between hematite (α-Fe_2O_3) and sapphire (α-Al_2O_3).[32] In the following growth period under a hydrogen atmosphere, released Fe atoms dope into TiO_2 and simultaneously trigger the release of lattice oxygen, with the oxygen release flux increasing by ~10^5. Successful experimental implementation of the LOT strategy requires four critical prerequisites: (1) preferential formation of stable TiO_2 on the substrate surface; (2) stable substitution of Fe atoms in the sapphire lattice; (3) controlled release of Fe atoms from sapphire under a reduction atmosphere; and (4) effective oxygen release and migration triggered by Fe doping. Therefore, the oxide catalyst must be a lattice-oxygen carrier with poor lattice matching with sapphire, and the dopant triggering the oxygen release should have good lattice matching with sapphire with controlled diffusion behavior, which constitutes the selection principle of ion implantation elements, as shown in Figure 1a.

Through the LOT strategy, s-SWCNT arrays with over 98% purity and negligible defects were successfully obtained, resulting in field effect transistors with outstanding performances of on/off ratio approaching 10^6, ultralow subthreshold swing of 60 mV/dec, and carrier mobility of up to 2291 $cm^2 \cdot V^{-1} \cdot s^{-1}$. Our LOT strategy not only provides new ideas for the controlled growth of s-SWCNT arrays but also opens an avenue for lattice-oxygen-based catalyst design, enabling significant advancements in nanotechnology.

RESULTS AND DISCUSSION

Catalyst and Dopant Design through Ion Implantation. To investigate the depth distribution of Ti and Fe in sapphire substrate after ion implantation, we conducted time-of-flight secondary ion mass spectrometry (TOF-SIMS), which is known as a powerful tool to carry out depth, two-dimensional (2D), and three-dimensional (3D) distribution of ionized elements and molecule fragments at the ppb level.[33−35] Based on the TOF-SIMS depth profile analysis in Figure 2a,b, the signal intensity of Ti and Fe both increased over time, peaking at 6−7 nm, followed by a gradual decrease, and the XPS depth profile analysis in Figure S1c−f showed the same trends. Monte Carlo simulation was also carried out using the stopping and range of ions in matter (SRIM)

https://doi.org/10.1021/jacs.5c08656
J. Am. Chem. Soc. 2025, 147, 32752−32760

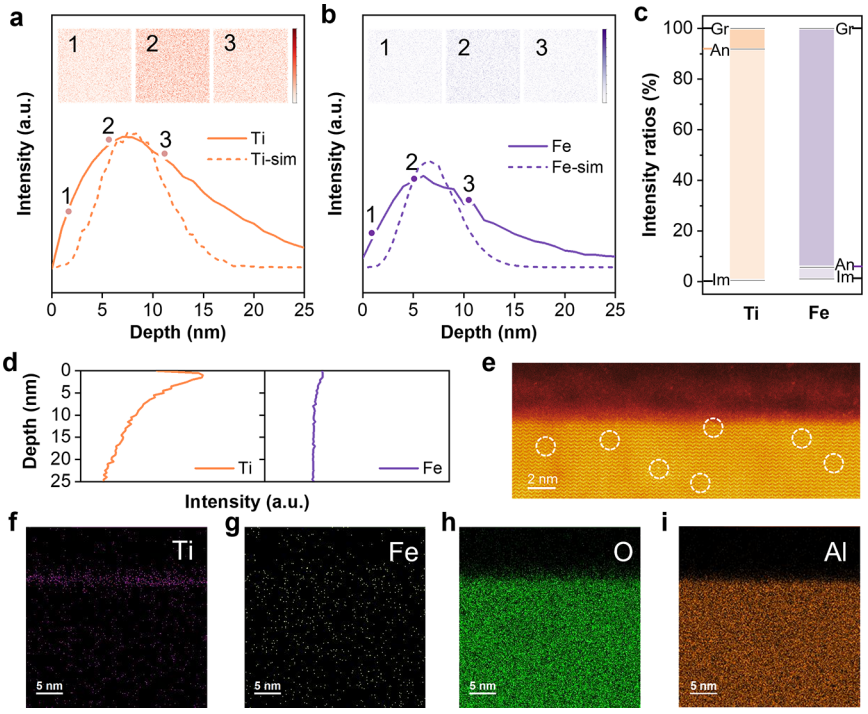

Figure 2. Distribution and migration behavior of Ti and Fe in TiFe/sapphire. (a, b) TOF-SIMS depth profiles and simulated ion distribution versus depth of (a) Ti and (b) Fe in as-prepared TiFe/sapphire, with insets showing corresponding 2D mapping images at 0−1, 4−5, and 10−11 nm, respectively (scale: 0 to maximum). (c) Divergent migration trends of Ti and Fe tracked through XPS across three stages: ion implantation (Im), annealing (An), and growth (Gr). (d) TOF-SIMS depth profiles of Ti and Fe components in annealed TiFe/sapphire. (e) Cross-sectional HAADF-STEM image of annealed TiFe/sapphire. (f−i) EDS mappings of (f) Ti, (g) Fe, (h) O, and (i) Al for the cross-sectional region.

computer program (dotted lines in Figure 2a,b), which matched well with the experimental data, confirming successful implantation of Ti and Fe ions into the sapphire substrate under designed energy parameters. Meanwhile, 2D TOF-SIMS mapping images of Ti and Fe (inset in Figure 2a,b) and 3D TOF-SIMS distribution images of Ti and Fe (Figure S1a,b) further demonstrated homogeneous in-plane distribution of both elements along *z*-axis, validating ion implantation's effectiveness for catalyst preloading.

Before CVD growth, air annealing was carried out to repair the surface damage induced by ion implantation radiation and to modify the distribution condition of Ti and Fe. Of interest here is that Ti and Fe have divergent migration trends in the annealing process due to the oxidation environment, as shown in the X-ray photoelectron spectroscopy (XPS) results in Figure 2c and Figure S2a,b. We designated the XPS signal obtained from samples after ion implantation, annealing, and growth process as Im, An, and Gr, respectively, using the growth signal intensity as the 100% reference. Notably, while only weak signal was observed after ion implantation due to the low content within the XPS detection depth, Ti signal emerged strongly in annealed samples, approaching the intensity after growth, indicating the substantial migration and precipitation of Ti upward to the sapphire surface in the process of annealing at 1100 °C[36,37] due to poor lattice matching with sapphire. By contrast, the Fe signal remained weak until the growth process under a reduced atmosphere, confirming Fe's thermodynamic stability within sapphire through partial Al substitution during the annealing process due to structural compatibility between hematite (α-Fe_2O_3) and sapphire (α-Al_2O_3), consistent with our previous study.[32] This differential behavior was corroborated by TOF-SIMS and XPS depth profiling (Figure 2d and Figure S2c−f), showing surface-concentrated Ti versus depth-invariant Fe distribution.

The distribution differences were further validated through the investigation of a cross-sectional sample along the $[1\bar{1}00]$ direction of sapphire by high-angle annular dark-field scanning transmission electron microscopy (HAADF-STEM). As shown in Figure 2e, an obvious contrast difference at the interface indicated element precipitation on the surface. In addition, reasonable atomic contrast variations (Figure S3) below the interface were detected, where brighter Z-contrast features (white circles) correspond to Fe substitutions in the sapphire lattice. Energy-dispersive spectrometer (EDS) mapping images in Figure 2f−i confirmed the enrichment of Ti element on the substrate surface (Figure 3f), correlating with TiO_2 formation (Ti^{4+} XPS in Figure S2a) in the process of air oxidation, and is consistent with the theoretically estimated thickness of the atomic layer from precipitated Ti to the substrate surface (Figure S4) at an appropriate dose of 1×10^{15} ions cm^{-2}. The surface topography of sapphire was also probed by atomic force microscopy (AFM) (Figure S5), showing a small height increase originating from TiO_2 formation after annealing. Different from the condition of Ti, the element distribution of Fe was discrete (Figure 2g), affirming that Fe atoms were homogeneously dispersed inside the sapphire, which is in accordance with the TOF-SIMS and STEM results.

Mechanism Analysis for the Lattice Oxygen Triggering Strategy. Through element design and annealing process, we achieved both catalyst preformation on the surface and dopant incorporation in the substrate. During the growth process in a reducing atmosphere, migration of Fe ions toward the surface enabled controlled doping of TiO_2 to facilitate lattice oxygen release. We investigated this oxygen-release

https://doi.org/10.1021/jacs.5c08656
J. Am. Chem. Soc. 2025, 147, 32752−32760

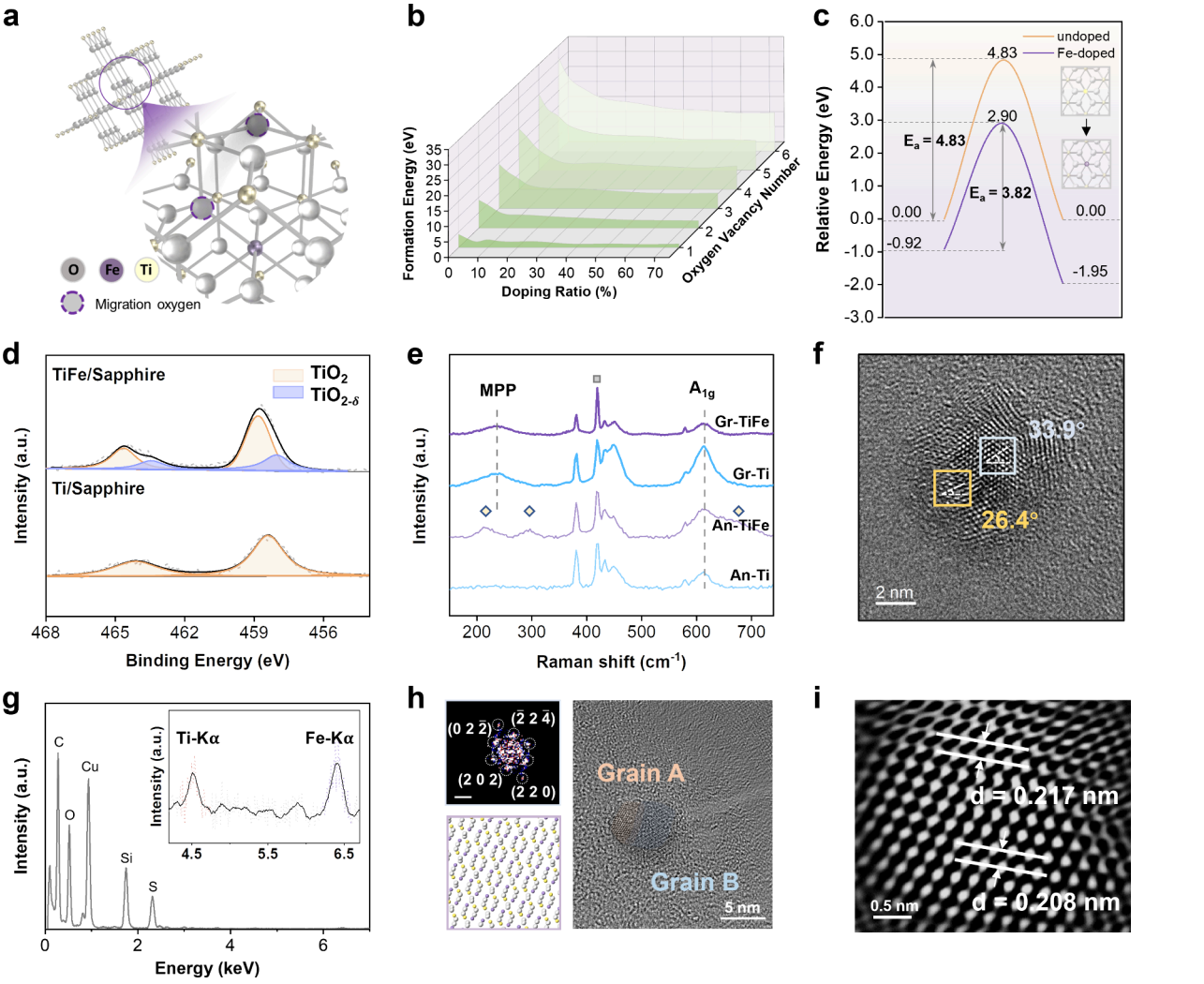

Figure 3. Theory calculations and characterizations of triggering lattice oxygen. (a) Schematic diagram of doping-triggered lattice oxygen migration. (b) Oxygen vacancy formation energies with the change of Fe doping ratio for different numbers of oxygen vacancies. (c) Relative energies along the oxygen migration pathway, both before and after Fe doping. (d) Ti 2p XPS spectra comparing undoped and Fe-doped systems. (e) Raman spectra of Ti/sapphire and TiFe/sapphire after annealing (An) and growth progress (Gr). (f) HAADF-STEM image with lattice distortion marked as blue and yellow squares. (g) EDS elemental composition of a catalyst nanoparticle with Ti and Fe. (h) HAADF-STEM image of an individual SWCNT grown from a catalyst nanoparticle, with the corresponding FFT pattern of the grain A (scale bar 5 1/nm) and atomic structure model (purple, yellow, and gray balls refer to Ti, Fe, and O atoms, respectively). (i) Distinct lattice spacings from lattice distortion of grain A in Figure 3h.

mechanism by density functional theory (DFT) calculations using the rutile lattice model (Figure 3a), which is the only thermodynamically stable phase of TiO_2.[38] Considering that Ti^{4+} and Fe^{3+} have similar ionic radii of 0.61 and 0.65 Å, respectively, Fe^{3+} ions can easily replace Ti^{4+} ions in the TiO_2 crystal lattice.[27] The computational results in Figure S6 suggest that the doping of TiO_2 by Fe^{3+}, especially substitutional doping, significantly decreases the formation energy (E_f) of oxygen vacancy (V_O). We further conducted a comprehensive thermodynamic analysis of the relationship between the substitutional dopant concentration and oxygen release characteristics (Figure S7), based on calculations of the total formation energy (Figure 3b) and sequential formation energy (Figure S8). With the increase in the Fe^{3+} doping concentration, both the total formation energy corresponding to different numbers of oxygen vacancies and the sequential formation energy of each single oxygen vacancy show a remarkable decline. For example, when the Fe doping concentration increases from 0 to 50%, the total formation energy for five oxygen vacancies decreases significantly from 25.3 to 10.3 eV, and the sequential formation energy drops from 5.4 to 2.7 eV. This clearly indicates that Fe^{3+} doping can effectively promote the release of oxygen. The obvious decreasing trend at varying concentrations also demonstrates a wide operational window for oxygen release. Remarkably, even when the Fe doping concentration is increased to only 3%, the energy required to generate one V_O is reduced by 33.7% (Figure S9).

We also investigated the effect of Fe-doping on oxygen release kinetics by calculating the energy barriers (E_a) of the potential migration pathways of lattice oxygen in the TiO_2 system before and after Fe-doping (Figure S10). For the tested pathway 1 (Figure 3c), in comparison with the 4.83 eV energy barrier in undoped TiO_2, Fe-doped TiO_2 exhibited a reduced barrier (E_a = 3.82 eV) from the Fe-bonded site to the Fe-nonbonded site, accompanied by a lower-energy initial state (E = −0.92 eV) and final state (E = −1.95 eV). These results indicate the enhanced feasibility of oxygen migration in Fe-

https://doi.org/10.1021/jacs.5c08656
J. Am. Chem. Soc. 2025, 147, 32752−32760

doped systems. Pathway 2 analysis yielded similar trends (Figure S11). It is worth noting that calculations of oxygen vacancy flux (Table S1) revealed a ~10^5-fold enhancement of lattice oxygen release for Fe-doped TiO_2 relative to undoped TiO_2. Collectively, these findings demonstrate that the formation and migration of oxygen vacancies in Fe-doped TiO_2 are both thermodynamically favorable and kinetically efficient, thus establishing preferential oxygen release pathways in Fe-doped TiO_2.

XPS results confirmed Ti valence reduction in surface TiO_2 after growth, as evidenced by the Ti 2p peak shifts in Figure 3d. Compared with the Ti/sapphire sample with only Ti^{4+} peaks at 464.2 eV ($2p_{1/2}$) and 458.4 eV ($2p_{3/2}$), the TiFe/sapphire sample displayed additional peaks at 463.4 and 458.0 eV, which are characteristic of oxygen-deficient TiO_2. This valence shift indicated that Fe doping was indispensable for the lattice oxygen release in TiO_2 during growth. The results of scaled-up H_2-TPR experiments in Figure S12 also indicate that the lattice oxygen of TiO_2 was significantly increased with Fe ion implantation, demonstrating the reliability of the LOT strategy.

Raman spectroscopy of the substrates revealed critical insights into the coordination structure and state of the sapphire surface (Figure 3e). Using α-Al_2O_3 A_{1g} mode at 419 cm^{-1} (marked with square label) as the normalized reference, we obtained spectra of Ti/sapphire and TiFe/sapphire sample after annealing and growth process with characteristic peaks (marked by corresponding mode names) at 230 and 610 cm^{-1}, representing the modes of the MPP (multiphoton process) and A_{1g} (antisymmetric bending vibration of O−Ti−O), respectively.[39] After exposure to growth atmosphere for 15 min, the intensity ratios of MPP to A_{1g} mode for TiFe/sapphire were higher than that for Ti/sapphire (Figure 3e), indicating increased coordinatively unsaturated sites in TiFe/sapphire, consistent with reported Raman spectra for Ti_2O_3/r-TiO_2 transition.[40] In addition, the disappearance of Raman peaks related to iron oxides and oxyhydroxides crystalline phases[41] (marked with rhombus label) in the TiFe/sapphire sample may be caused by the fine dispersion of these within TiO_2 matrices. These results align with the above theoretical predictions about oxygen release profiting from Fe doping into TiO_2.

The uniform dispersion on the substrate of postgrowth catalyst nanoparticles was observed (Figure S13), originating from high temperature dewetting.[42] We performed STEM characterization to further investigate the catalyst nanoparticles. Atomic-level alterations in various titanium−iron oxide structures indicated that the selectivity originated not from the lattice matching of carbon nanotubes and the catalyst with a specific structure.[43] Titanium carbide (TiC)[44] formation was excluded as TiO_2 conversion into TiC requires significantly harsher conditions than those employed for CNT growth, consistent with the absence of TiC nanoparticles in STEM characterization. The lattice plane angles of 26.4 and 33.9° in nanoparticles (Figure 3f) confirmed the presence of oxygen-deficient lattice distortion,[45,46] supported by the well-defined bright spots of fast Fourier transform (FFT) diffraction patterns (Figure S14) deriving from corresponding lattice fringes in blue and golden boxes. Observed fuzzy features and weak FFT pattern rings (Figure S15) further suggested lattice disorder or amorphization, characteristic of considerable oxygen vacancy concentration.[47,48]

The coexistence of Ti and Fe in the catalyst nanoparticle was determined by EDS (Figure 3g, Table S2) and corresponding spatial mapping images (Figure S16). For a nanoparticle connected to an individual SWCNT containing two crystallized grains (marked by two different colors) (Figure 3h and Figure S17), FFT diffraction patterns identified the grain A along $[1\bar{1}1]$ as $FeTiO_3$ and the grain B along $[1\bar{1}0]$ as Fe_3C, both matching well with the corresponding atomic models. In non-nucleating $FeTiO_3$ grain, the lattice distortion region displayed two distinct lattice spacings (0.217 and 0.208 nm) marked by white line (Figure 3i), deviating from the 0.210 nm spacing of $FeTiO_3$ (2 0 2). This structural discrepancy aligns with oxygen vacancy-induced cation separation and structure variation.[46]

Growth Results and Device Performances of SWNT Arrays. Under optimal conditions, lattice oxygen release induced the enrichment of s-SWCNTs (Figure 4a). Scanning electron microscopy (SEM) images in Figure 4b revealed Fe dose-dependent etching enhancement of TiFe/sapphire catalysts, evidenced by shortened SWCNTs. The similar etching condition emerged with different Ti dose (Figure S18). Sustained lattice oxygen release during growth enabled by the consecutive distribution of Fe atoms in depth persistently etched m-SWCNTs and suppressed their growth.

Raman line mapping spectra in Figure 4c and Figure S19 validated the universal efficacy of triggered-oxygen assisted etching for m-SWCNTs removal, with m-/s-SWCNTs identified by radical breathing mode (RBM) peak positions based on Kataura plot.[49] Controlled Ti/Fe dosing on sapphire elucidated the LOT mechanism: Compared with the maximum s-SWCNT enrichment proportion of 98%, Ti-only samples exhibited limited s-SWCNT enrichment due to inadequate lattice oxygen release, consistent with Figure 4b observations. Conversely, excessive Fe/Ti ratios reduced selectivity as isolated Fe catalyst nanoparticles generated m-SWCNTs, matching the theoretical calculation results of doping saturation effects until there was no selectivity with natural 1/3 m-SWCNTs for Fe-only samples.

Electrical performances of TiFe/sapphire-grown SWCNT arrays were characterized via back-gated field-effect transistors (FETs) fabricated on SiO_2/Si substrates with a 1 μm channel length (L_{ch}) (Figure S20). The transfer characteristics and the corresponding on/off ratios (Figure 4d,e and Figure S21) revealed that 54 of the measured 55 FET devices exhibited semiconducting behavior, confirming >98% s-SWCNT purity, in accordance with Raman statistics in Figure 4c. The on/off ratios of 64% of the FET devices exceeded 10^3, where the maximum on/off ratio reached 10^5. Raman line mapping spectra under 532 nm laser excitation of the SWCNT arrays in Figure 4f showed negligible D-band signals, confirming the high crystallinity of the carbon nanotubes. In addition, top-gated FET devices with a single SWCNT in channels (Figure 4g inset: L_{ch} = 1 μm with a 4 nm HfO_2 dielectric layer) achieved near-ideal performances of on/off ratio approaching 10^6 and subthreshold swing (SS) of 60 mV dec^{-1} (Figure 4g,h), the room temperature theoretical limit, which demonstrates that the SWCNTs grown by LOT method were perfectly crystalline and defect-negligible. Using the standard carrier mobility formula:

$$\mu = \frac{L_{ch} g_m}{W_{ch} C_G V_{ds}} \quad (1)$$

https://doi.org/10.1021/jacs.5c08656
J. Am. Chem. Soc. 2025, 147, 32752−32760

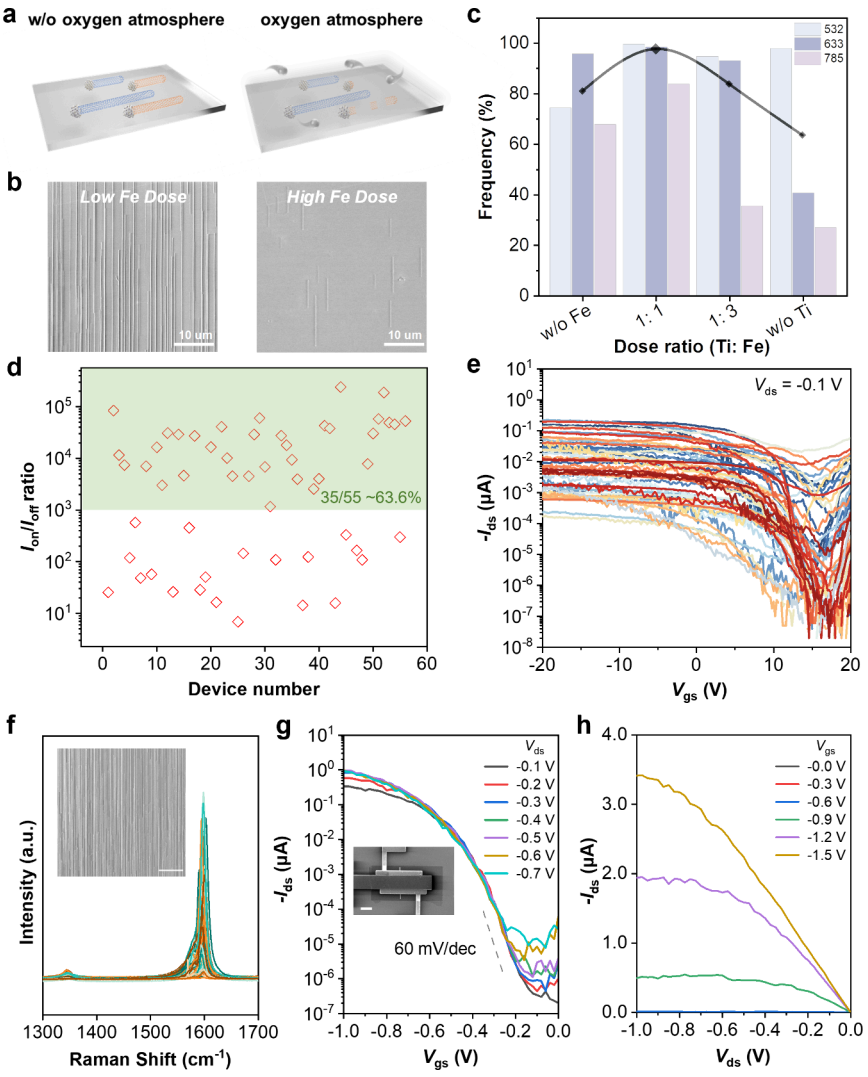

Figure 4. Etching of lattice oxygen and electrical characterization of s-SWCNT arrays. (a) Schematic diagram for selectively etching of lattice oxygen, where the blue and orange nanotubes denote s-SWCNTs and m-SWCNTs, respectively. (b) SEM images of SWCNT arrays with different Fe implantation doses, under the noniron-dominant catalyst condition. (c) Raman analysis of the abundance of s-SWCNTs with different contents of Fe. (d) Transfer characteristics and (e) on/off ratio statistics of the measured FET devices based on s-SWCNT arrays. (f) Raman spectra of s-SWCNT arrays (inset: SEM image of the SWCNT arrays). (g) Transfer characteristics (inset: SEM image of the FET) and (h) output characteristics of the FET. Scale bars, 20 μm (SEM image in f) and 1 μm (SEM image in g).

we obtained a carrier mobility of up to 2291 $cm^2 \cdot V^{-1} \cdot s^{-1}$. These results demonstrated the exceptional electrical properties of our SWCNTs for carbon-based integrated circuits.

CONCLUSIONS

In summary, this study presents a lattice oxygen triggering strategy to achieve horizontally aligned SWCNT arrays with >98% semiconducting SWCNT purity. By coimplanting Ti and Fe ions into sapphire substrates and annealing, Fe atoms dope into TiO_2 under a reducing growth atmosphere and promote lattice oxygen release. This enables precise oxidative etching of m-SWCNTs and the enrichment of s-SWCNTs. DFT calculations confirm Fe doping significantly reduces oxygen vacancy formation energy and facilitates kinetic oxygen release (~10^5-fold enhancement of lattice-oxygen release flux). The resulting SWCNT arrays exhibit exceptional electrical performance of on/off ratios up to 10^6, an ultralow subthreshold swing of 60 mV dec^{-1}, and a carrier mobility of 2291 $cm^2 \cdot V^{-1} \cdot s^{-1}$. The LOT strategy decouples catalyst doping and growth processes, offering a scalable and compatible approach for high-purity s-SWCNT synthesis in industrial production. Further study is needed to understand lattice oxygen behavior (e.g., charge transfer effects) and to optimize etching conditions for improved utilization. In a broader view, the versatile LOT strategy, with a universal catalyst synthesis approach through sequential ion implantation and suitable postprocessing, provides new insights into multimetal catalyst design and doping tuning.

METHODS

Preparation of Ion Implantation Samples. The Ti and Fe ion implantation at sapphire substrates was conducted at room temperature by employing a home-built ion implanter (FM-400). The ion energy was set as 9 keV, and the ion dose of Ti and Fe was set as the range from 1×10^{14} to 1×10^{16} ions cm^{-2}, respectively. After ion implantation, the annealing process at 1100 °C in air for 5 h was conducted as an indispensable procedure.

Growth of SWCNT Arrays. The sapphire substrates were placed in a quartz tube with polished surfaces upward. The 300 sccm argon

https://doi.org/10.1021/jacs.5c08656
J. Am. Chem. Soc. 2025, 147, 32752−32760

was first introduced into the tube from the entrance until the temperature reached 850 °C. Then, hydrogen (100−500 sccm) and ethanol were introduced into the reactor for SWCNT growth. After growth for 10−20 min, the furnace was cooled to room temperature in an argon and hydrogen atmosphere.

Transfer of SWCNT Arrays. The sample film was transferred onto the ultrathin carbon support film (EMCN, BZ11032b) by a standard wet transfer method using an etching solution (2.5 mol/L potassium hydroxide solution) to dissolve the sapphire glass substrates, followed by a standard stripping process of PMMA. The sample film was transferred onto a Si/SiO_2 (300 nm) substrate for back-gated FET and top-gated FET using a similar method.

FIB Detail. Focused ion beam methods (FIB, using a TESCAN Solaris FIB dual beam SEM) were used to prepare a cross-sectional sample. To avoid the damage of the ion beam, the sample was coated with a thick layer of carbon. Then, trenching milling was performed initially at 20 nA and then at 10 and 2.5 nA for polishing until a trench was prepared, followed by a lamella sample cut and transferred to copper grids. Next, the lamella was first polished by an ion beam at 250 and 150 pA under 30 kV until its thickness was less than 200 nm. Finally, the lamella was polished to about 30 nm thick by ion beam at 20 pA under 2 kV with over and under tilting below 2°.

Characterizations and Measurements. SEM images were obtained on a Hitachi SU8220 SEM operated at 1 kV and 15 nA with a working distance of 8 mm. Raman spectra of CNTs were collected from Jovin Yvon-Horiba LabRam systems with 532, 633, and 785 nm excitation (beam spot of ∼1 μm). X-ray photoelectron spectroscopy (XPS) was performed on an AXIS Supra X-ray photoelectron spectrometer (Kratos Analytical Ltd.) with Al Kα (1486.6 eV) as the X-ray source. XPS depth analysis was performed on a Thermo Scientific K-Alpha XPS with Al Kα (1486.6 eV) as the X-ray source, and the sputter etching was performed using an Ar^+ beam. Atomic force microscope (AFM) images were obtained using a Dimension Icon microscope (Bruker). TOF-SIMS measurements were conducted with a PHI nano TOF II instrument (ULVAC-PHI Inc., Japan). A Bi_3^{+2} (a small cluster of three Bi atoms with two charges) beam (30 kV) was used as the primary beam to detect the samples, and the sputter etching was performed using an Ar^+ beam (3 kV) with the analysis area of 20 × 20 μm^2. HAADF-STEM images and EDS mappings of cross-section sapphire sample and catalyst nanoparticle sample on copper grid were acquired using an aberration-corrected JEM-ARM300F operated at 300 kV. Therein, moderate underfocus was needed for the observation of catalyst nanoparticles.

SRIM Simulations. The simulations were based on stopping and the range of ions in matter (SRIM) computer program. Specifically, in the prerequisite setting of sapphire as a target, the ion distribution versus implantation depth of Ti and Fe with 9 keV was calculated by the Monte Carlo method.

DFT Calculation Details. The details are available in the Supporting Information.

Fabrication and Measurements of FET Devices. For back-gate FET devices, the FET pad and contact were formed on the transferred samples by the electron beam lithography (EBL) process, and deposition of Pd/Au film (20 nm/40 nm) was done via electron beam evaporation (EBE) followed by a standard lift-off process.

For top-gate FET devices, after the FET pad and contact were formed, the channel area was defined by EBL, and redundant CNTs were removed by reaction ion etching (RIE) with 60 sccm oxygen flow and 40 W ratio frequency generator power for 20 s. Then, the gate dielectric layer for FET was patterned via EBL, and HfO_2 film of 4 nm thickness was grown via atomic layer deposition (ALD) at 105 °C, followed by a standard lift-off process. Finally, the deposition of Ti/Au film (5 nm/40 nm) on the designed gate region by EBL and standard lift-off process was proceeded. Electrical characterizations were performed using a semiconductor device analyzer B1500A and a probe station at room temperature under atmospheric conditions.

■ ASSOCIATED CONTENT

Supporting Information

The Supporting Information is available free of charge at https://pubs.acs.org/doi/10.1021/jacs.5c08656.

Additional DFT calculation details, ion implantation analysis, ion implantation results, DFT results, material characterizations, and FET performance, including Tables S1 and S2 and Figures S1−S21 (PDF)

■ AUTHOR INFORMATION

Corresponding Authors

Xiucai Sun − *Beijing Graphene Institute (BGI), Beijing 100094, China*; Email: sunxc@bgi-graphene.com

Liu Qian − *School of Materials Science and Engineering, Peking University, Beijing 100871, China*; Email: qianliu-cnc@pku.edu.cn

Jin Zhang − *Beijing Science and Engineering Center for Nanocarbons, Beijing National Laboratory for Molecular Sciences, College of Chemistry and Molecular Engineering and School of Materials Science and Engineering, Peking University, Beijing 100871, China*; orcid.org/0000-0003-3731-8859; Email: jinzhang@pku.edu.cn

Authors

Zhe Liu − *Beijing Science and Engineering Center for Nanocarbons, Beijing National Laboratory for Molecular Sciences, College of Chemistry and Molecular Engineering and School of Materials Science and Engineering, Peking University, Beijing 100871, China*

Hao Li − *Beijing Graphene Institute (BGI), Beijing 100094, China; School of Instrument and Electronics, North University of China, Taiyuan 030051, China*

Zhisheng Peng − *School of Materials Science and Engineering, Peking University, Beijing 100871, China*

Mingzhi Zou − *Beijing Science and Engineering Center for Nanocarbons, Beijing National Laboratory for Molecular Sciences, College of Chemistry and Molecular Engineering, Peking University, Beijing 100871, China*

Zhenghang Yu − *Department of Electronics, Peking University, Beijing 100871, China*

Yue Li − *School of Materials Science and Engineering, Peking University, Beijing 100871, China*

Zanlin Qiu − *School of Materials Science and Engineering, Peking University, Beijing 100871, China*

Complete contact information is available at: https://pubs.acs.org/10.1021/jacs.5c08656

Author Contributions

The manuscript was written through contributions of all authors. All authors have given approval to the final version of the manuscript.

Notes

The authors declare no competing financial interest.

■ ACKNOWLEDGMENTS

This work was financially supported by the Ministry of Science and Technology of China (2022YFA1203302 and 2022YFA1203304), the National Natural Science Foundation of China (grant nos. 52021006, 22494641, and 52102032), the Strategic Priority Research Program of CAS (XDB36030100), the Beijing National Laboratory for Molecular Sciences (BNLMS-CXTD-202001), the Shenzhen Science and Tech-

nology Innovation Commission (KQTD20221101115627004), the Postdoctoral Fellowship Program of CPSF (GZC20230034), and the China Postdoctoral Science Foundation (2024M750091). The authors thank Prof. Chenguang Qiu from Peking University for his technical support in device fabrication.

REFERENCES

(1) Grimaud, A.; Diaz-Morales, O.; Han, B.; Hong, W. T.; Lee, Y.-L.; Giordano, L.; Stoerzinger, K. A.; Koper, M. T. M.; Shao-Horn, Y. Activating lattice oxygen redox reactions in metal oxides to catalyse oxygen evolution. *Nat. Chem.* **2017**, *9* (5), 457−465.
(2) Binninger, T.; Mohamed, R.; Waltar, K.; Fabbri, E.; Levecque, P.; Kötz, R.; Schmidt, T. J. Thermodynamic explanation of the universal correlation between oxygen evolution activity and corrosion of oxide catalysts. *Sci. Rep.* **2015**, *5* (1), 12167.
(3) Jacob, M.; Nguyen, H.; Raj, R.; Garcia-Barriocanal, J.; Hong, J.; Perez-Aguilar, J. E.; Hoffman, A. S.; Mkhoyan, K. A.; Bare, S. R.; Neurock, M.; Bhan, A. Selective chemical looping combustion of acetylene in ethylene-rich streams. *Science* **2025**, *387* (6735), 744−749.
(4) Grätzel, M. Photoelectrochemical cells. *Nature* **2001**, *414* (6861), 338−344.
(5) Hoffmann, M. R.; Martin, S. T.; Choi, W.; Bahnemann, D. W. Environmental Applications of Semiconductor Photocatalysis. *Chem. Rev.* **1995**, *95* (1), 69−96.
(6) Yang, D.; Liu, H.; Zheng, Z.; Yuan, Y.; Zhao, J.-c.; Waclawik, E. R.; Ke, X.; Zhu, H. An Efficient Photocatalyst Structure: TiO_2(B) Nanofibers with a Shell of Anatase Nanocrystals. *J. Am. Chem. Soc.* **2009**, *131* (49), 17885−17893.
(7) Yu, H.; Irie, H.; Shimodaira, Y.; Hosogi, Y.; Kuroda, Y.; Miyauchi, M.; Hashimoto, K. An Efficient Visible-Light-Sensitive Fe(III)-Grafted TiO_2 Photocatalyst. *J. Phys. Chem. C* **2010**, *114* (39), 16481−16487.
(8) Lin, D.; Yu, Y.; Li, L.; Zou, M.; Zhang, J. Growth of Semiconducting Single-Walled Carbon Nanotubes Array by Precisely Inhibiting Metallic Tubes Using ZrO_2 Nanoparticles. *Small* **2021**, *17* (48), No. e2006605.
(9) Qin, X.; Peng, F.; Yang, F.; He, X.; Huang, H.; Luo, D.; Yang, J.; Wang, S.; Liu, H.; Peng, L.; Li, Y. Growth of semiconducting single-walled carbon nanotubes by using ceria as catalyst supports. *Nano Lett.* **2014**, *14* (2), 512−517.
(10) Franklin, A. D. The road to carbon nanotube transistors. *Nature* **2013**, *498* (7455), 443−444.
(11) Hills, G.; Lau, C.; Wright, A.; Fuller, S.; Bishop, M. D.; Srimani, T.; Kanhaiya, P.; Ho, R.; Amer, A.; Stein, Y.; Murphy, D.; Arvind; Chandrakasan, A.; Shulaker, M. M. Modern microprocessor built from complementary carbon nanotube transistors. *Nature* **2019**, *572* (7771), 595−602.
(12) Liu, L.; Han, J.; Xu, L.; Zhou, J.; Zhao, C.; Ding, S.; Shi, H.; Xiao, M.; Ding, L.; Ma, Z.; Jin, C.; Zhang, Z.; Peng, L.-M. Aligned, high-density semiconducting carbon nanotube arrays for high-performance electronics. *Science* **2020**, *368* (6493), 850−856.
(13) He, M.; Zhang, S.; Zhang, J. Horizontal Single-Walled Carbon Nanotube Arrays: Controlled Synthesis, Characterizations, and Applications. *Chem. Rev.* **2020**, *120* (22), 12592−12684.
(14) Ze, Y.; Liu, Y.; Wang, B.; Yin, H.; Jin, C.; Zhang, Z. Carbon nanotube materials for future integrated circuit applications. *Mater. Today* **2024**, *79*, 97−111.
(15) Zhao, X.; Gao, N.; Zhang, Z.; Liu, Q.; Sheng, J.; Hu, Y.; Li, R.; Xu, H.; Peng, L.; Li, Y. Selective growth of semiconducting single-walled carbon nanotubes solely from carbon monoxide. *Nano Res.* **2023**, *16* (11), 12720−12726.
(16) Zhang, G.; Qi, P.; Wang, X.; Lu, Y.; Li, X.; Tu, R.; Bangsaruntip, S.; Mann, D.; Zhang, L.; Dai, H. Selective etching of metallic carbon nanotubes by gas-phase reaction. *Science* **2006**, *314* (5801), 974−977.
(17) Zhou, W.; Zhan, S.; Ding, L.; Liu, J. General Rules for Selective Growth of Enriched Semiconducting Single Walled Carbon Nanotubes with Water Vapor as in Situ Etchant. *J. Am. Chem. Soc.* **2012**, *134* (34), 14019−14026.
(18) Ding, L.; Tselev, A.; Wang, J.; Yuan, D.; Chu, H.; McNicholas, T. P.; Li, Y.; Liu, J. Selective Growth of Well-Aligned Semiconducting Single-Walled Carbon Nanotubes. *Nano Lett.* **2009**, *9* (2), 800−805.
(19) Li, P.; Zhang, J. Sorting out semiconducting single-walled carbon nanotube arrays by preferential destruction of metallic tubes using water. *J. Mater. Chem.* **2011**, *21* (32), 11815−11821.
(20) Yu, B.; Liu, C.; Hou, P. X.; Tian, Y.; Li, S.; Liu, B.; Li, F.; Kauppinen, E. I.; Cheng, H. M. Bulk synthesis of large diameter semiconducting single-walled carbon nanotubes by oxygen-assisted floating catalyst chemical vapor deposition. *J. Am. Chem. Soc.* **2011**, *133* (14), 5232−5235.
(21) Huang, Y.; Yu, Y.; Yu, Y.; Zhang, B. Oxygen Vacancy Engineering in Photocatalysis. *Sol. RRL* **2020**, *4* (8), 2000037.
(22) Pan, X.; Yang, M.-Q.; Fu, X.; Zhang, N.; Xu, Y.-J. Defective TiO_2 with oxygen vacancies: synthesis, properties and photocatalytic applications. *Nanoscale* **2013**, *5* (9), 3601−3614.
(23) Chen, X.; Liu, L.; Huang, F. Black titanium dioxide (TiO_2) nanomaterials. *Chem. Soc. Rev.* **2015**, *44* (7), 1861−1885.
(24) Wang, X. H.; Li, J. G.; Kamiyama, H.; Katada, M.; Ohashi, N.; Moriyoshi, Y.; Ishigaki, T. Pyrogenic Iron(III)-Doped TiO2 Nanopowders Synthesized in RF Thermal Plasma: Phase Formation, Defect Structure, Band Gap, and Magnetic Properties. *J. Am. Chem. Soc.* **2005**, *127* (31), 10982−10990.
(25) Wu, Q.; van de Krol, R. Selective Photoreduction of Nitric Oxide to Nitrogen by Nanostructured TiO_2 Photocatalysts: Role of Oxygen Vacancies and Iron Dopant. *J. Am. Chem. Soc.* **2012**, *134* (22), 9369−9375.
(26) Zhao, Y.; Zhao, Y.; Shi, R.; Wang, B.; Waterhouse, G. I. N.; Wu, L.; Tung, C.; Zhang, T. Tuning Oxygen Vacancies in Ultrathin TiO_2 Nanosheets to Boost Photocatalytic Nitrogen Fixation up to 700 nm. *Adv. Mater.* **2019**, *31* (16), 1806482.
(27) Wu, Q.; Zheng, Q.; van de Krol, R. Creating Oxygen Vacancies as a Novel Strategy To Form Tetrahedrally Coordinated Ti^{4+} in Fe/TiO_2 Nanoparticles. *J. Phys. Chem. C* **2012**, *116* (12), 7219−7226.
(28) Wang, G.; Zhang, M.; Chen, D.; Guo, Q.; Feng, X.; Niu, T.; Liu, X.; Li, A.; Lai, J.; Sun, D.; Liao, Z.; Wang, Y.; Chu, P. K.; Ding, G.; Xie, X.; Di, Z.; Wang, X. Seamless lateral graphene p−n junctions formed by selective in situ doping for high-performance photodetectors. *Nat. Commun.* **2018**, *9* (1), 5168.
(29) Zhao, Y.; li, Y.; Chen, Y.; Chen, Y.; Zhou, D.; Zhao, Z. Ion implantation assisted synthesis of graphene on various dielectric substrates. *Nano Res.* **2021**, *14* (5), 1280−1286.
(30) Xie, Y.; Li, Y.; Peng, Z.; Wang, C.; Qiu, Z.; Cai, X.; Song, T.; Si, J.; Zhao, X.; Qian, L.; Zhao, Z.; Zhang, J. Nano-seeding catalysts for high-density arrays of horizontally aligned carbon nanotubes with wafer-scale uniformity. *Nat. Commun.* **2025**, *16* (1), 149.
(31) Dalpian, G. M.; Chelikowsky, J. R. Self-Purification in Semiconductor Nanocrystals. *Phys. Rev. Lett.* **2006**, *96* (2), No. 226802.
(32) Hu, Y.; Kang, L.; Zhao, Q.; Zhong, H.; Zhang, S.; Yang, L.; Wang, Z.; Lin, J.; Li, Q.; Zhang, Z.; Peng, L.; Liu, Z.; Zhang, J. Growth of high-density horizontally aligned SWNT arrays using Trojan catalysts. *Nat. Commun.* **2015**, *6* (1), 6099.
(33) Ma, C.; Xu, F.; Song, T. Dual-Layered Interfacial Evolution of Lithium Metal Anode: SEI Analysis via TOF-SIMS Technology. *ACS Appl. Mater. Interfaces* **2022**, *14* (17), 20197−20207.
(34) Bai, Y.; Huang, Z.; Zhang, X.; Lu, J.; Niu, X.; He, Z.; Zhu, C.; Xiao, M.; Song, Q.; Wei, X.; Wang, C.; Cui, Z.; Dou, J.; Chen, Y.; Pei, F.; Zai, H.; Wang, W.; Song, T.; An, P.; Zhang, J.; Dong, J.; Li, Y.; Shi, J.; Jin, H.; Chen, P.; Sun, Y.; Li, Y.; Chen, H.; Wei, Z.; Zhou, H.; Chen, Q. Initializing film homogeneity to retard phase segregation for stable perovskite solar cells. *Science* **2022**, *378* (6621), 747−754.
(35) Deng, C.; Yang, B.; Liang, Y.; Zhao, Y.; Gui, B.; Hou, C.; Shang, Y.; Zhang, J.; Song, T.; Gong, X.; Chen, N.; Wu, F.; Chen, R. Bipolar Polymeric Protective Layer for Dendrite-Free and Corrosion-

https://doi.org/10.1021/jacs.5c08656
J. Am. Chem. Soc. 2025, 147, 32752−32760

Resistant Lithium Metal Anode in Ethylene Carbonate Electrolyte. *Angew. Chem., Int. Ed.* **2024**, *63* (17), No. e202400619.
(36) Naramoto, H.; McHargue, C. J.; White, C. W.; Williams, J. M.; Holland, O. W.; Abraham, M. M.; Appleton, B. R. Near surface modification of α-Al_2O_3 by ion implantation followed by thermal annealing. *Nucl. Instrum. Methods Phys. Res.* **1983**, *209−210*, 1159−1166.
(37) Naramoto, H.; White, C. W.; Williams, J. M.; McHargue, C. J.; Holland, O. W.; Abraham, M. M.; Appleton, B. R. Ion implantation and thermal annealing of α-Al2O3 single crystals. *J. Appl. Phys.* **1983**, *54* (2), 683−698.
(38) Bak, T.; Sherif, S. A.; Black, D. S.; Nowotny, J. Defect Chemistry of Titanium Dioxide (Rutile). *Progress Toward Sustainable Energy. Chem. Rev.* **2024**, *124* (21), 11848−11914.
(39) Li, L.; Yan, J.; Wang, T.; Zhao, Z.-J.; Zhang, J.; Gong, J.; Guan, N. Sub-10 nm rutile titanium dioxide nanoparticles for efficient visible-light-driven photocatalytic hydrogen production. *Nat. Commun.* **2015**, *6* (1), 5881.
(40) Li, Y.; Yang, Y.; Shu, X.; Wan, D.; Wei, N.; Yu, X.; Breese, M. B. H.; Venkatesan, T.; Xue, J. M.; Liu, Y.; Li, S.; Wu, T.; Chen, J. From Titanium Sesquioxide to Titanium Dioxide: Oxidation-Induced Structural, Phase, and Property Evolution. *Chem. Mater.* **2018**, *30* (13), 4383−4392.
(41) de Faria, D. L. A.; Venâncio Silva, S.; de Oliveira, M. T. Raman microspectroscopy of some iron oxides and oxyhydroxides. *J. Raman Spectrosc.* **1997**, *28* (11), 873−878.
(42) Fiawoo, M. F. C.; Bonnot, A. M.; Amara, H.; Bichara, C.; Thibault-Pénisson, J.; Loiseau, A. Evidence of Correlation between Catalyst Particles and the Single-Wall Carbon Nanotube Diameter: A First Step towards Chirality Control. *Phys. Rev. Lett.* **2012**, *108* (19), No. 195503.
(43) Zhang, S.; Kang, L.; Wang, X.; Tong, L.; Yang, L.; Wang, Z.; Qi, K.; Deng, S.; Li, Q.; Bai, X.; Ding, F.; Zhang, J. Arrays of horizontal carbon nanotubes of controlled chirality grown using designed catalysts. *Nature* **2017**, *543* (7644), 234−238.
(44) Koc, R.; Folmer, J. S. Carbothermal synthesis of titanium carbide using ultrafine titania powders. *J. Mater. Sci.* **1997**, *32* (12), 3101−3111.
(45) Di Valentin, C.; Pacchioni, G.; Selloni, A. Electronic Structure of Defect States in Hydroxylated and Reduced Rutile Surfaces. *Phys. Rev. Lett.* **2006**, *97* (16), No. 166803.
(46) Qu, J.; Liu, W.; Liu, R.; He, J.; Liu, D.; Feng, Z.; Feng, Z.; Li, R.; Li, C. Evolution of oxygen vacancies in cerium dioxide at atomic scale under CO_2 reduction. *Chem. Catal.* **2023**, *3* (10), No. 100759.
(47) Naldoni, A.; Allieta, M.; Santangelo, S.; Marelli, M.; Fabbri, F.; Cappelli, S.; Bianchi, C. L.; Psaro, R.; Dal Santo, V. Effect of Nature and Location of Defects on Bandgap Narrowing in Black TiO_2 Nanoparticles. *J. Am. Chem. Soc.* **2012**, *134* (18), 7600−7603.
(48) Chen, X.; Liu, L.; Yu, P. Y.; Mao, S. S. Increasing Solar Absorption for Photocatalysis with Black Hydrogenated Titanium Dioxide Nanocrystals. *Science* **2011**, *331* (6018), 746−750.
(49) Kataura, H.; Kumazawa, Y.; Maniwa, Y.; Umezu, I.; Suzuki, S.; Ohtsuka, Y.; Achiba, Y. Optical properties of single-wall carbon nanotubes. *Synth. Met.* **1999**, *103* (1), 2555−2558.

https://doi.org/10.1021/jacs.5c08656
J. Am. Chem. Soc. 2025, 147, 32752−32760